Inorganic Chemistry

Article

pubs.acs.org/IC

# Coordination Effects on Electron Distributions for Rhodium Complexes of the Redox-Active Bis(3,5-di-*tert*-butyl-2-phenolate) amide Ligand

Géza Szigethy, David W. Shaffer, and Alan F. Heyduk*

Department of Chemistry, University of California, Irvine, California 92697, United States

Supporting Information

**ABSTRACT:** New rhodium complexes of bis(3,5-di-*tert*-butyl-2-phenol)amine ([ONO$^{cat}$]H$_3$) were synthesized, and their electronic properties were investigated. These compounds were prepared by combining [ONO$^{q}$]K and [(cod)Rh($\mu$-Cl)]$_2$ in the presence of an auxiliary donor ligand to yield complexes of the type [ONO]RhL$_n$ ($n$ = 3, L = py (**1**); $n$ = 2, L = PMe$_3$ (**2a**), L = PMe$_2$Ph (**2b**), PMePh$_2$ (**2c**), PPh$_3$ (**2d**)). Single-crystal X-ray diffraction studies on [ONO]Rh(py)$_3$ (**1**) revealed a six-coordinate, octahedral rhodium complex. In the case of [ONO]Rh(PMe$_3$)$_2$ (**2a**), X-ray diffraction showed a five-coordinate, distorted square-pyramidal coordination environment around the rhodium center. While **1** is static on the NMR time scale, complexes **2a**−**d** are fluxional, displaying both rapid isomerization of the square-pyramidal structure and exchange of coordinated and free phosphine ligands. UV−vis spectroscopy shows stark electronic differences between **1** and **2a**−**d**. Whereas **1** displays a strong absorbance at 380 nm with a much weaker band at 585 nm in the absorption spectrum, complexes **2a**−**d** display an intense ($\varepsilon > 10^4$ M$^{-1}$ cm$^{-1}$), low-energy absorption band in the region 580−640 nm; however, in the cases of **2a** and **2b**, the addition of excess phosphine resulted in changes to the UV−vis spectrum indicating the formation of six-coordinate adducts [ONO]Rh(PMe$_3$)$_3$ (**3a**) and [ONO]Rh(PMe$_2$Ph)$_3$ (**3b**), respectively. The experimental and DFT computational data for the six-coordinate complexes **1**, **3a**, and **3b** are consistent with their formulation as classical, d$^6$, pseudo-octahedral, coordination complexes. In the five-coordinate complexes **2a**−**2d**, $\pi$-bonding between the rhodium center and the [ONO] ligand leads to a high degree of covalency and metal−ligand electron distributions that are not accurately described by formal oxidation state assignments.

## INTRODUCTION

Ligands capable of adopting more than one stable oxidation state have earned the designation as redox-active or non-innocent because of their propensity to complicate the electronic properties and reactivity of the metal center to which they are bound.[1−3] Installation of these ligands onto independently redox-active metals further hinders the characterization of valence-electron distribution in the resultant complexes, while simultaneously providing access to electronic structures uncommon in more classical metal−ligand complexes.[4−8] Perhaps the most common redox-active ligands are the catecholates and their *ortho*-aminophenolate and *ortho*-diamide analogues, whose metal complexes are known to exhibit rich redox chemistry independent of the coordinated metal ion.[8−10] Expansion of the catecholate platform into polydentate, poly-aromatic geometries makes ligand redox potentials more accessible than in less conjugated systems while also decreasing the lability of the ligand in its oxidized form.[11−14] These properties, combined with the potential for ligand modification, make expanded catecholate-type ligands attractive for a wide range of reaction chemistry.

One redox-active ligand whose reactivity and electronic characteristics have been extensively studied on both transition metals and main group elements is the tridentate [ONO] ligand ([ONO$^{cat}$]H$_3$ = bis(3,5-di-*tert*-butyl-2-phenol)amine).[15] While capable of binding metals in a doubly deprotonated, facially coordinating form {([ONO]H)$^{2-}$},[16−18] the [ONO] ligand is most commonly studied in its fully deprotonated form, which results in a meridional coordination mode. The fully deprotonated form of the [ONO] ligand can adopt one of three formal oxidation states: the reduced catecholate form, [ONO$^{cat}$]$^{3-}$, the one-electron oxidized semiquinonate form, [ONO$^{sq\bullet}$]$^{2-}$, or the two-electron oxidized quinonate form, [ONO$^{q}$]$^{-}$, as shown in Scheme 1. Most studies of the [ONO] platform have focused on

**Scheme 1**

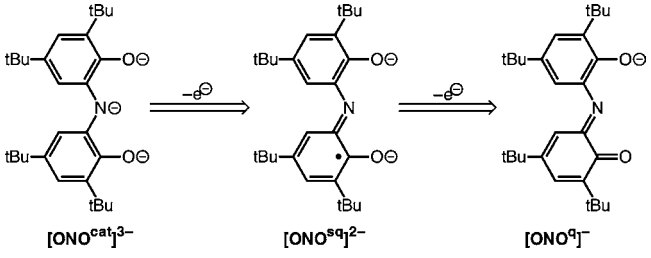


the structural and electronic characteristics of coordinatively saturated M[ONO]$_2$ complexes,[15,16,19−24] but more recently, investigations have turned toward the synthesis and reactivity of heteroleptic M[ONO]L$_n$ complexes,[18,25] which includes alkyl-migration on tin,[26] copper-catalyzed oxidation,[27] and stoichiometric

**Received:** December 3, 2011
**Published:** April 6, 2012

   dx.doi.org/10.1021/ic2026076 | *Inorg. Chem.* 2012, 51, 12606−12618

oxidative addition/reductive elimination transformations on tantalum.[28−30]

Research in our group explores the unique electronic interactions and chemical transformations accessible to metal complexes with redox-active ligands, especially in cases where the reactivity can be attributed explicitly to the redox properties of the ligand.[11,13,14,28,29,31−36] Our prior investigations of [ONO] complexes have focused on early transition metal ions with $d^0$ electron configurations,[28−30] but the possibility of complementary redox reactivity between the [ONO] ligand and electron-rich late transition metals prompted an investigation of the coordination chemistry of the [ONO] ligand with rhodium. Rhodium complexes display a rich reaction chemistry and are capable of a wide variety of stoichiometric and catalytic bond-activation reactions,[37,38] including the activation of classically unreactive small molecules such as $H_2$, $CO_2$,[39] $N_2$,[40] and even $CH_4$.[41] The coordination chemistry of rhodium with redox-active ligands remains relatively unexplored, although our studies on the rhodium complex [nacnac]Rh(phdi) (nacnac$^-$ = $\beta$-diketiminate, phdi = phenanthrenediimine) indicated a close energetic match between rhodium and ligand valence orbitals, resulting in significant noninnocent ligand behavior.[40,42−44]

This investigation details the first installation of the [ONO] ligand onto rhodium and the physical and electronic characterization of the resultant complexes. Synthesis of [ONO]Rh complexes was facilitated through the use of the potassium salt of the oxidized [ONO] ligand, [ONO$^q$]K, which is an as-yet unreported starting material for [ONO] complexes. Through a combination of UV−visible spectroscopy, solution titrations, and density functional theory (DFT) calculations it was determined that [ONO]Rh complexes exhibit noninnocent electronic behavior that is strongly influenced by the coordination of ancillary ligands on the rhodium center. In coordinatively saturated six-coordinate complexes, well-defined [ONO$^{cat}$]$^-$Rh$^{III}$L$_3$ complexes were obtained (L = pyridine, PR$_3$). In five-coordinate [ONO]RhL$_2$ complexes (L = PR$_3$), a high-degree of covalency in metal−ligand $\pi$-bonding results in valence electron distributions that are intermediate between [ONO$^{cat}$]Rh$^{III}$ and [ONO$^{sq}$]Rh$^{II}$ electronic configurations.

## EXPERIMENTAL SECTION

**General Considerations.** Compounds described herein are oxygen and moisture sensitive, so manipulations were carried out under a nitrogen atmosphere using standard Schlenk or glovebox techniques. Solvents were purified by sparging with argon followed by sequential passage through activated Q5 and alumina columns to remove oxygen and water, respectively. Reagents were purchased from commercial sources and used as received with the exception of [ONO$^{cat}$]H$_3$[29] and [(cod)Rh($\mu$-Cl)]$_2$,[45] which were synthesized following literature procedures.

**Spectroscopic Methods.** NMR spectra were collected on a Bruker DRX 500 MHz ($^1$H 500 MHz, $^{13}$C 128 MHz) or a Bruker DRX400 ($^1$H 400 MHz, $^{31}$P 162 MHz) spectrometer at 298 K in $C_6D_6$ unless otherwise noted. The NMR solvent was degassed by several freeze−pump−thaw cycles, dried over sodium benzophenone ketyl radical, and vacuum-distilled before use. All $^1$H, $^{13}$C{$^1$H}, and $^{31}$P{$^1$H} chemical shifts are reported using the standard $\delta$-scale in ppm. The $^1$H and $^{13}$C{1H} NMR spectra were referenced to TMS using the proteo- and natural abundance $^{13}$C impurities in $C_6D_6$ (7.15 and 128.02 ppm). $^{31}$P{$^1$H} NMR spectra were referenced to $H_3PO_4$ using the Ξ (Xi) scale and the residual proton impurities $C_6D_6$.[46] FTIR spectra were recorded with a Perkin−Elmer Spectrum One spectrophotometer as KBr pellets. UV−visible spectra were recorded with a Perkin-Elmer Lambda 800 spectrometer in 1-cm quartz cuvettes in dry, degassed benzene. Electrospray Ionization (ESI) mass spectrometry was performed on a Waters LCT Premier mass spectrometer.

**[ONO$^q$]K.** Just-thawed tetrahydrofuran (THF, 35 mL) was added to a combination of [ONO]H$_3$ (2.00 g, 4.70 mmol, 1 equiv) and KH (565 mg, 1.41 mmol, 3 equiv) in a 100 mL round-bottom flask. The mixture was stirred at room temperature overnight while $H_2$ gas was released. The resulting yellow, turbid solution was frozen, and PhI(OAc)$_2$ (1.51 g, 4.70 mmol, 1 equiv) was added. The solution turned purple/black with further evolution of $H_2$ gas. The mixture was stirred at room temperature for 6 h. Solid KOAc was removed by filtration and washed with THF until washes were nearly colorless. The solvent was removed from the combined filtrates under vacuum, coevaporated with toluene, then twice with pentane, resulting in 1.99 g of product as a black powder (92%). Anal. Calcd. (Found) for $C_{28}H_{40}NO_2K$ (%): C, 72.82 (72.56); H, 8.73 (9.10); N, 3.03 (2.89). $^1$H NMR (500 MHz) $\delta$/ppm: 1.27 (s, C$H_3$, 18H), 1.48 (s, C$H_3$, 18H), 7.22 (s, br, aryl-*H*, 2H), 7.31 (s, br, aryl-*H*, 2H). $^{13}$C NMR (125 MHz) $\delta$/ppm: 30.65 (CH$_3$), 34.58 (CCH$_3$), 35.63 (CCH$_3$), 118.53 (aryl-*C*), 130.88 (aryl-*C*), 139.95 (aryl-*C*), 144.21 (aryl-*C*), 145.27 (aryl-*C*), 179.45 (aryl-*C*). UV−vis ($C_6H_6$) $\lambda_{max}$/nm ($\varepsilon$/M$^{-1}$ cm$^{-1}$): 346 (5,330), 537 (1,930), 810 (16,100). MS (ESI−) *m*/*z*: 422.2 (M−), 883.5 ($M_2$K−).

**[ONO$^{cat}$]Rh(py)$_3$, 1.** A solution of [ONO$^q$]K (187 mg, 0.406 mmol, 1 equiv) in 18 mL of Et$_2$O was frozen, and then [(cod)Rh($\mu$-Cl)]$_2$ (100 mg, 0.203 mmol, 0.5 equiv) and pyridine (131 $\mu$L, 1.62 mmol, 4 equiv) were added. The mixture was stirred for 4 h at room temperature. Solvent was removed under vacuum from the brown suspension, and the residue was extracted with 35 mL of toluene and filtered. Removal of solvent from the filtrate under vacuum and coevaporation with pentane yielded 306 mg (99%) of the product as a fine brown solid. X-ray quality crystals were grown by diffusion of pentane into a THF solution at room temperature. Anal. Calcd. (Found) for $C_{43}H_{35}N_4O_2Rh$ (%): C, 67.70 (67.47); H, 7.27 (7.17); N, 7.34 (7.12). $^1$H NMR (500 MHz): $\delta$ 1.54 (s, C$H_3$, 18H), 2.13 (s, C$H_3$, 18H), 6.03 (t, py-*H*, *J* = 8.5 Hz, 4H), 6.28−6.31 (m, py-*H*, 4H), 6.53−6.57 (m, py-*H*, 1H), 7.05 (s, aryl-*H*, 2H), 8.16 (s, aryl-*H*, 2H), 8.76 (d, py-*H*, *J* = 6.5 Hz, 4H), 9.16 (d, py-*H*, *J* = 6.0 Hz, 2H). The low solubility of **1** precluded the acquisition of a $^{13}$C{$^1$H} NMR spectrum. UV−vis ($C_6H_6$) $\lambda_{max}$/nm ($\varepsilon$/M$^{-1}$ cm$^{-1}$): 380 (23,900), 585 (1,300). MS (ESI+) *m*/*z*: 762.6 (M+), 763.6 (MH+).

**General Synthesis of [ONO]Rh(PR$_3$)$_2$, 2a−d.** A solution of [ONO$^q$]K (0.20−0.25 mmol, 1 equiv) in 15 mL of Et$_2$O was frozen, and [(cod)Rh($\mu$-Cl)]$_2$ (0.5 equiv) and phosphine (2 equiv) were added. The mixture was stirred at room temperature for at least 4 h. The teal/blue solution was filtered, and solvent was removed under vacuum. The residue was in all cases clean enough for subsequent reaction with near-quantitative yields (greater than 95%). Analytical samples were purified further by recrystallization as described below.

**[ONO]Rh(PMe$_3$)$_2$, 2a.** Blue/black crystalline solid isolated in several crops from pentane solutions at −35 °C, 61%. Anal. Calcd. (Found) for $C_{34}H_{58}NO_2P_2Rh$ (%): C, 60.26 (60.03); H, 8.63 (8.43); N, 2.07 (1.98). $^1$H NMR (500 MHz): $\delta$ 0.90 (vt, P−C$H_3$, $J_{app}$ = 6.0 Hz, 18H), 1.62 (s, C$H_3$, 18H), 1.80 (s, C$H_3$, 18H), 7.49 (d, aryl-*H*, *J* = 1.5 Hz, 2H), 8.70 (s, aryl-*H*, 2H). $^{13}$C{$^1$H} NMR (125 MHz): $\delta$ 16.37 (vt, P-CH$_3$, $J_{app}$ = 13.8 Hz), 30.61(CH$_3$), 32.58 (CH$_3$), 34.88 (CCH$_3$), 35.76 (CCH$_3$), 111.74 (aryl-*C*), 116.26 (vt, aryl-*C*, $J_{app}$ = 2.4 Hz), 137.45 (aryl-*C*), 137.90 (aryl-*C*), 144.83 (vt, aryl-*C*, $J_{app}$ = 6.6 Hz), 166.23 (vt, aryl-*C*, $J_{app}$ = 5.5 Hz). $^{31}$P{$^1$H} NMR (162 MHz): $\delta$ 18.80 (d, *P*Me$_3$, $^1J_{Rh-P}$ = 137.9 Hz). UV−vis ($C_6H_6$) $\lambda_{max}$/nm ($\varepsilon$/M$^{-1}$ cm$^{-1}$): 321 (17,600), 396 (2,970), 587 (10,300). MS (ESI+) *m*/*z*: 677.0 (M+), 678.0 (MH+).

**[ONO]Rh(PMe$_2$Ph)$_2$, 2b.** Blue/black crystalline solid from saturated pentane at −35 °C, 57%. Anal. Calcd. (Found) for $C_{44}H_{62}NO_2P_2Rh$ (%): C, 65.91 (66.19); H, 7.79 (8.17); N, 1.75 (1.89). $^1$H NMR (500 MHz): $\delta$ 1.10 (vt, P−C$H_3$, $J_{app}$ = 6.0 Hz, 12H), 1.63 (s, C$H_3$, 18), 1.86 (s, C$H_3$, 18H), 6.92−6.99 (m, aryl-*H*, 6H), 7.17−7.19 (m, aryl-*H*, 4H), 7.56 (d, aryl-*H*, *J* = 1.5 Hz, 2H), 8.63 (s, aryl-*H*, 2H). $^{13}$C{$^1$H} NMR (125 MHz): $\delta$ 14.35 (vt, P-CH$_3$, $J_{app}$ = 14.1 Hz), 30.62 (CH$_3$), 32.57 (CH$_3$), 34.89 (CCH$_3$), 35.78 (CCH$_3$), 112.38 (aryl-*C*), 116.96 (aryl-*C*), 129.67 (aryl-*C*), 130.32 (vt, aryl-*C*,


dx.doi.org/10.1021/ic2026076 | Inorg. Chem. 2012, 51, 12606−12618

**Table 1. X-ray Data Collection and Refinement Parameters for $[ONO^{cat}]Rh(py)_3$ (1) and $[ONO]Rh(PMe_3)_2$ (2a)**

| | $[ONO^{cat}]Rh(py)_3$·4 THF·1/2 $C_5H_{12}$ (**1**·4 THF·1/2 $C_5H_{12}$) | $[ONO]Rh(PMe_3)_2$·1/2 $C_5H_{12}$ (**2a**·1/2 $C_5H_{12}$) |
|---|---|---|
| empirical formula | $C_{104.5}H_{148}N_8O_8Rh_2$ | $C_{36.5}H_{64}NO_2P_2Rh$ |
| formula weight | 1850.13 | 713.74 |
| crystal system | orthorhombic | monoclinic |
| space group | *Pbca* | $P2_1/c$ |
| *T*, K | 83(2) | 143(2) |
| *a*, Å | 22.4517(10) | 13.8702(12) |
| *b*, Å | 28.7074(12) | 23.903(2) |
| *c*, Å | 31.8954(14) | 13.4550(12) |
| $\alpha$ | 90° | 90° |
| $\beta$ | 90° | 118.0260(10)° |
| $\gamma$ | 90° | 90° |
| *V*, Å$^3$ | 20557.5(15) | 3937.7(6) |
| *Z* | 8 | 4 |
| reflections collected | 217984 | 42307 |
| data/restraints/parameters | 21056/20/1102 | 8074/0/419 |
| R1 [$I > 2\sigma(I)$][a] | 0.0475 | 0.0450 |
| wR2 (all data)[a] | 0.1322 | 0.0830 |
| GOF[a] | 1.042 | 1.020 |

[a] $R1 = \sum||F_o| - |F_c||/\sum|F_o|$; $wR2 = [\sum w(F_o^2 - F_c^2)^2/\sum w(F_o^2)^2]^{1/2}$; $GOF = [\sum w(|F_o| - |F_c|)^2/(n - m)]^{1/2}$.

$J_{app}$ = 4.6 Hz), 136.2−136.6 (vm, aryl-*C*), 137.76 (aryl-*C*), 138.45 (aryl-*C*), 144.97 (vt, aryl-*C*, $J_{app}$ = 7.1 Hz), 166.59 (vt, aryl-*C*, $J_{app}$ = 5.6 Hz). $^{31}P\{^1H\}$ NMR (162 MHz): $\delta$ 24.44 (d, *P*Me$_2$Ph, $^1J_{Rh-P}$ = 137.7 Hz). UV−vis ($C_6H_6$) $\lambda_{max}$/nm ($\varepsilon$/M$^{-1}$ cm$^{-1}$): 323 (19,400), 416 (3,080), 625 (12,300). MS (ESI+) *m*/*z*: 800.9 (M+), 802.0 (MH+).

**[ONO]Rh(PMePh$_2$)$_2$, 2c.** Teal, amorphous powder from saturated pentane at −35 °C, 88%. Anal. Calcd. (Found) for $C_{54}H_{66}NO_2P_2Rh$ (%): C, 70.04 (69.80); H, 7.18 (7.33); N, 1.51 (1.50). $^1H$ NMR (500 MHz): $\delta$ 1.57 (s, C*H*$_3$, 18H), 1.62 (s, br, P−C*H*$_3$, 6H), 1.76 (s, C*H*$_3$, 18H), 6.83−6.89 (m, aryl-*H*, 12H), 7.27 (m, br, aryl-*H*, 8H), 7.53 (s, aryl-*H*, 2H), 8.37 (s, aryl-*H*, 2H). $^{13}C\{^1H\}$ NMR (125 MHz): $\delta$ 12.56 (P-*C*H$_3$), 30.80 (*C*H$_3$), 32.50 (*C*H$_3$), 34.70 (*C*CH$_3$), 35.67 (*C*CH$_3$), 113.42 (aryl-*C*), 118.09 (aryl-*C*), 129.72 (aryl-*C*), 132.27 (aryl-*C*), 133.92 (vt, aryl-*C*, $J_{app}$ = 5.6 Hz), 135.13 (vt, aryl-*C*, $J_{app}$ = 21.0 Hz), 137.62 (aryl-*C*), 138.77 (aryl-*C*), 145.39 (aryl-*C*), 167.86 (aryl-*C*). $^{31}P\{^1H\}$ NMR (162 MHz): $\delta$ 38.35 (d, *P*MePh$_2$, $^1J_{Rh-P}$ = 137.7 Hz). UV−vis ($C_6H_6$) $\lambda_{max}$/nm ($\varepsilon$/M$^{-1}$ cm$^{-1}$): 319 (18,100), 626 (11,000). MS (ESI+) *m*/*z*: 924.9 (M+), 925.9 (MH+).

**[ONO]Rh(PPh$_3$)$_2$, 2d.** Blue/black, microcrystalline hairs of the hemietherate isolated in several crops by layering a saturated Et$_2$O solution under pentane at −35 °C, 85%. Anal. Calcd. (Found) for $C_{64}H_{70}NO_2P_2Rh$·1/2($C_4H_{10}O$) (%): C, 72.92 (71.33); H, 6.95 (6.76); N, 1.29 (1.15). $^1H$ NMR (500 MHz): $\delta$ 1.11 (t, Et$_2$O−C*H*$_3$, *J* = 7.0 Hz, 3H), 1.53 (s, C*H*$_3$, 36 H), 3.26 (q, Et$_2$O−C*H*$_2$, *J* = 7.0 Hz, 2H), 6.81 (t, aryl-*H*, *J* = 7.5 Hz, 12H), 6.89 (t, aryl-*H*, *J* = 7.5 Hz, 6H), 7.36 (q, aryl-*H*, *J* = 7.0 Hz, 12H), 7.51 (d, aryl-*H*, *J* = 2.0 Hz, 2H), 8.55 (d, aryl-*H*, *J* = 2.0 Hz, 2H). $^{13}C\{^1H\}$ NMR (125 MHz,): $\delta$ 15.58 (Et$_2$O-*C*H$_3$), 30.95 (*C*H$_3$), 32.34 (*C*H$_3$), 34.74 (*C*CH$_3$), 35.49 (*C*CH$_3$), 65.90 (Et$_2$O-*C*H$_2$), 114.13 (aryl-*C*), 119.80 (vt, aryl-*C*, $J_{app}$ = 4.6 Hz), 128.09 (aryl-*C*), 129.70 (aryl-*C*), 134.04 (vt, aryl-*C*, $J_{app}$ = 20.3 Hz), 134.76 (vt, aryl-*C*, $J_{app}$ = 4.8 Hz), 137.66 (aryl-*C*), 139.69 (vt, aryl-*C*, $J_{app}$ = 4.5 Hz), 146.67 (aryl-*C*), 168.98 (vd, aryl-*C*, $J_{app}$ = 7.0 Hz). $^{31}P\{^1H\}$ NMR (162 MHz): $\delta$ 57.47 (d, *P*Ph$_3$, $^1J_{Rh-P}$ = 139.2 Hz). UV−vis ($C_6H_6$) $\lambda_{max}$/nm ($\varepsilon$/M$^{-1}$ cm$^{-1}$): 315 (18,100), 446 (4,600), 639 (11,800). MS (ESI+) *m*/*z*: 1049.0 (M+), 1050.0 (MH+).

**Comproportionation of 2a and 2b.** Recrystallized **2a** (4.8 mg, 0.0071 mmol) and **2b** (5.6 mg, 0.0070 mmol) were dissolved in 0.75 mL of $C_6D_6$ and transferred to an NMR tube. NMR analysis indicated the presence of minor amounts of **2a** and **2b** with the primary product being $[ONO]Rh(PMe_3)(PMe_2Ph)$, the characteristic peaks of which are listed below. $^1H$ NMR (400 MHz): $\delta$ 0.53 (d, P−C*H*$_3$, $J_{app}$ = 12.8 Hz, 9H), 1.47 (d, P−C*H*$_3$, *J* = 10.4 Hz, 6H), 1.62 (s, C*H*$_3$, 18H), 1.85 (s, C*H*$_3$, 18H), 7.05−7.10 (m, arom. *H*, 2H), 7.53 (s, arom. *H*, 2H), 7.77−7.81 (m, arom. *H*, 2H), 8.74 (s, arom. *H*, 2H). $^{31}P\{^1H\}$ NMR (162 MHz): $\delta$ 13.70 (dd, *P*Me$_3$, $^1J_{Rh-P}$ = 119.4 Hz, $^3J_{P-P}$ = 65.3 Hz), 29.66 (dd, *P*Me$_2$Ph, $^1J_{Rh-P}$ = 155.8 Hz, $^3J_{P-P}$ = 65.3 Hz). MS (ESI+) *m*/*z*: 739.20 (M+).

**Electrochemical Methods.** Electrochemical experiments were performed on a Gamry Series G 300 Potentiostat/Galvanostat/ZRA (Gamry Instruments, Warminster, PA, U.S.A.) using a 3.0 mm glassy carbon working electrode, a platinum wire auxiliary electrode, and a silver wire reference electrode. Electrochemical experiments were performed at ambient temperature (20−24 °C), in a nitrogen-filled glovebox. Tetrabutylammonium hexafluorophosphate (Acros) was recrystallized from ethanol three times and dried under vacuum before use. Commercially available $[CoCp_2][PF_6]$ was dried under vacuum for 1 day before use. Analyte concentrations were 1.0 mM in THF with 0.10 M $[NBu_4][PF_6]$ as the supporting electrolyte. All potentials are referenced to $[Cp_2Fe]^{+/0}$, using $[Cp_2Co][PF_6]$ as an internal standard (−1.34 V vs $[Cp_2Fe]^{+/0}$).[47]

**X-ray Diffraction.** X-ray diffraction data were collected on crystals mounted on glass fibers using a Bruker CCD platform diffractometer equipped with a CCD detector. Measurements were carried out using Mo K$_\alpha$ ($\lambda$ = 0.71073 Å) radiation, which was wavelength selected with a single-crystal graphite monochromator. A full sphere of data was collected for each crystal structure. The APEX2 program package was used to determine unit-cell parameters and to collect data.[48] The raw frame data were processed sing SAINT[49] and SADABS[50] to yield the reflection data files. Subsequent calculations were carried out using the SHELXTL[51] program suite. Structures were solved by direct methods and refined on $F^2$ by full-matrix least-squares techniques to convergence. Analytical scattering factors for neutral atoms were used throughout the analyses.[52] Hydrogen atoms, though visible in the difference Fourier map, were generated at calculated positions and their positions refined using the standard riding models. ORTEP diagrams were generated using ORTEP-3 for Windows,[53] and all thermal ellipsoids are drawn at the 50% probability level. Diffraction collection and refinement data are shown in Table 1.

**Titrations.** Stock solutions of $[ONO]Rh(PR_3)_2$ were prepared by dissolving a known mass of the complex accurate to 0.1 mg in benzene in a volumetric flask. A 0.10 M stock solution of $PMe_3$ in toluene was prepared by diluting 1.00 mL of commercially available 1.0 M $PMe_3$ solution in toluene to 10 mL with toluene in a volumetric flask. These stock solutions were stored at −35° when not in use. Titrations were conducted by two different methods, yielding the analogous results.

*Method 1.* Appropriate aliquots of the $[ONO]Rh(PR_3)_2$ and $PR_3$ stock solutions were added to a series of 5 or 10 mL volumentric flasks to generate solutions that were 40−50 $\mu$M in metal complex and with


dx.doi.org/10.1021/ic2026076 | *Inorg. Chem.* 2012, 51, 12606−12618

the desired concentration of free phosphine upon dilution to the volume mark. The samples were allowed to equilibrate for at least 30 min before acquisition of the UV–vis spectra.

*Method 2.* A 50 mL solution of [ONO]Rh($PR_3$)$_2$ in benzene was made in a 50 mL volumetric flask and transferred to an Erlenmeyer flask. Successive 5 mL aliquots of this solution were removed after each addition of $PR_3$. Samples for both titration methods were allowed to equilibrate at least 30 min before measurement, although color change was immediate upon addition of $PR_3$. Titrations were repeated three times to verify reproducibility.

**Titration Data Treatment.** Spectrophotometric titration data were analyzed using the program Hyperquad2003[54,55] utilizing non-linear least-squares regression to determine formation constants. The absorption spectrum of the starting {[ONO]Rh} complex was determined by the absorption spectrum of the first sample in the titration, to which no titrant was added. Wavelengths between 290–750 nm were typically used for data refinement.

**Density Functional Theory Calculations.** All calculations were performed using the TURBOMOLE program package.[56] The geometric and electronic structures were optimized without symmetry constraints using the B3LYP functional[57−60] and a polarized triple-$\zeta$ basis set (TZVP).[61] All molecules were treated in the gas phase without accounting for solvent. The energy was converged to $10^{-7}$ Hartree. Natural population analyses[62] and plots were also obtained at the B3LYP/TZVP level; the contour values were 0.045 for the molecular orbital plots.

## RESULTS

**[ONO$^q$]K Synthesis and Metalation.** To leverage the wealth of available rhodium(I) starting materials, a reliable [ONO$^q$]$^-$ synthon was targeted. The proteo species [ONO$^q$]H has been reported by the condensation of 3,5-di-*tert*-butyl-*o*-quinone and 2-hydroxy-3,5-di-*tert*-butylaniline,[18] but in our hands this reaction was unreliable and typically gave cyclized products.[63] The Zn[ONO$^q$]$_2$ complex has also been used as a source for the [ONO$^q$]$^-$ ligand,[26] but to avoid reliance on metathesis of a tridentate ligand, a scalable synthesis of the potassium salt [ONO$^q$]K was developed. According to eq 1, deprotonation of [ONO$^{cat}$]H$_3$ with KH followed by two-electron oxidation with PhI(OAc)$_2$, yielded [ONO$^q$]K in yields of greater than 90%. Three equivalents of KH are added at the beginning of the reaction; however, removal of the third, nitrogen-bound proton does not seem to occur until addition of the oxidant in the second step. The [ONO$^q$]K salt is purple/black, significantly soluble in most organic solvents, and stable under a nitrogen atmosphere at room temperature. While $^n$BuLi could be substituted for KH in the above synthesis, the resultant [ONO$^q$]Li salt exhibits a much broader $^1$H NMR signal than the potassium salt, making purity more difficult to verify. While [ONO$^{cat}$]H$_3$ is colorless, the absorption spectrum of [ONO$^q$]K is characterized by a strong, broad band at 810 nm (Figure 1). This feature is very similar to those reported for purple [ONO$^q$]H as well as for M[ONO$^q$]$_2$ complexes of transition metal and main group elements.[20]

$$[ONO^{cat}]H_3 \xrightarrow[\substack{-3\ H_2\\ -2\ KOAc}]{\substack{i.\ 3\ KH\\ ii.\ PhI(OAc)_2}} [ONO^q]K + PhI \qquad (1)$$

Successful transmetalation of [ONO$^q$]K with rhodium(I) starting materials required the inclusion of neutral donor ligands to saturate the rhodium coordination sphere in the product. As shown in Scheme 2, the reaction of 2 equiv of [ONO$^q$]K with [(cod)Rh($\mu$-Cl)]$_2$ in the presence of pyridine resulted in quantitative formation of [ONO$^{cat}$]Rh(py)$_3$ (**1**) as a brown solid. Reactions using monodentate phosphine ligands afforded the blue-green phosphine adducts [ONO]Rh($PR_3$)$_2$ ($PR_3$ = $PMe_3$, **2a**; $PR_3$ = $PMe_2Ph$, **2b**; $PR_3$ = $PMePh_2$, **2c**; $PR_3$ = $PPh_3$, **2d**) in quantitative yields.

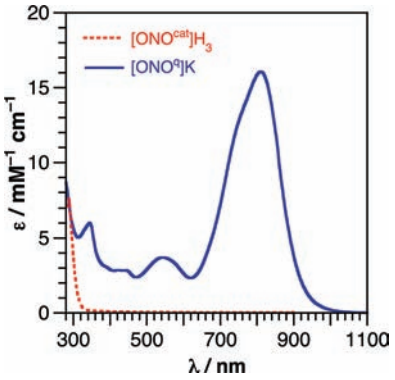


**Figure 1.** UV–vis absorption spectra of [ONO$^{cat}$]H$_3$ and [ONO$^q$]K acquired in $C_6H_6$ at 298 K.

**Scheme 2**

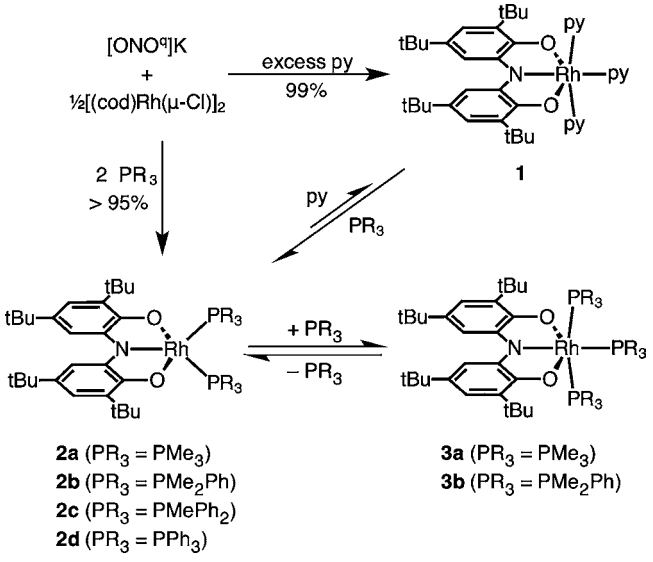


**Crystallographic Characterization.** To identify the rhodium coordination environment in complexes **1** and **2**, single-crystal X-ray diffraction studies were performed. With the exception of **2c**, all rhodium complexes could be isolated as crystalline solids; however, the crystals typically suffered from rapid desolvation, allowing only **1** and **2a** to be structurally characterized by single-crystal X-ray diffraction. Selected metrical parameters for **1** and **2a** are listed in Table 2, and the structures of the rhodium complexes are illustrated in Figure 2. In both structures the [ONO] ligand is coordinated in the expected meridional fashion. The [ONO]–Rh metal–ligand bond lengths are similar in the two structures, and these distances are consistent with Rh–O/N bond lengths reported for rhodium(III) complexes with polydentate ligands.[64−66]

The crystal structures in Figure 2 illustrate two different coordination geometries: **1** adopts a six-coordinate octahedral geometry while **2a** adopts a distorted square-pyramidal geometry. The rhodium coordination environment and Rh–N(py) bond distances in **1** are similar to those in *mer*-RhCl$_3$(py)$_3$,[67] with the largest deviations from regular octahedral geometry deriving from the acute (84°) bite angles inherent to the [ONO] ligand. In the case of **2a**, a more relaxed geometry about the metal center is observed. The rhodium in **2a** sits 0.28 Å above the mean-squared


dx.doi.org/10.1021/ic2026076 | *Inorg. Chem.* 2012, 51, 12606–12618

**Table 2. Selected Crystallographic/Computational Bond Distances (Å) for [ONO$^{cat}$]Rh(py)$_3$ (1), [ONO]Rh(PMe$_3$)$_2$ (2a), [ONO]Rh(PPh$_3$)$_2$ (2d), and [ONO$^{cat}$]Rh(PMe$_3$)$_3$ (3a)**

| | Bond Lengths / Å | | | |
|---|---|---|---|---|
| 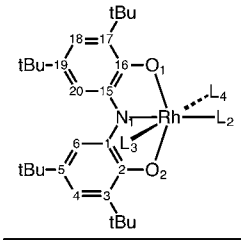 | [ONO$^{cat}$]Rh(py)$_3$ **1**$^{a,b}$ | [ONO]Rh(PMe$_3$)$_2$ **2a**$^{c}$ | [ONO]Rh(PPh$_3$)$_2$ **2d**$^{c}$ | [ONO$^{cat}$]Rh(PMe$_3$)$_3$ **3a**$^{c}$ |
| Rh(1)–O(1) | 2.015(2) / 2.032 | 1.999(2) / 2.032 | -- / 2.072 | -- / 2.051 |
| Rh(1)–O(2) | 2.021(2) / 2.033 | 2.010(2) / 2.036 | -- / 2.065 | -- / 2.054 |
| Rh(1)–N(1) | 1.939(3) / 1.951 | 1.940(3) / 1.954 | -- / 1.941 | -- / 2.000 |
| Rh(1)–L(2) | 2.075(3) / 2.144 | 2.2744(9) / 2.326 | -- / 2.402 | -- / 2.374 |
| Rh(1)–L(3) | 2.062(3) / 2.104 | 2.1938(9) / 2.253 | -- / 2.347 | -- / 2.415 |
| Rh(1)–L(4) | 2.062(3) / 2.075 | -- / -- | -- / -- | -- / 2.408 |
| C(2)–O(1) | 1.357(4) / 1.359 | 1.349(4) / 1.330 | -- / 1.321 | -- / 1.352 |
| C(16)–O(2) | 1.363(4) / 1.358 | 1.342(4) / 1.328 | -- / 1.323 | -- / 1.354 |
| C(1)–N(1) | 1.385(4) / 1.391 | 1.401(4) / 1.396 | -- / 1.391 | -- / 1.390 |
| C(15)–N(1) | 1.391(4) / 1.389 | 1.399(4) / 1.395 | -- / 1.394 | -- / 1.389 |
| C(1)–C(2) | 1.441(4) / 1.431 | 1.421(4) / 1.432 | -- / 1.429 | -- / 1.439 |
| C(2)–C(3) | 1.401(4) / 1.410 | 1.403(4) / 1.417 | -- / 1.424 | -- / 1.408 |
| C(3)–C(4) | 1.404(5) / 1.400 | 1.394(4) / 1.394 | -- / 1.390 | -- / 1.405 |
| C(4)–C(5) | 1.387(5) / 1.394 | 1.390(4) / 1.399 | -- / 1.403 | -- / 1.388 |
| C(5)–C(6) | 1.396(4) / 1.392 | 1.388(4) / 1.390 | -- / 1.384 | -- / 1.399 |
| C(6)–C(1) | 1.402(4) / 1.402 | 1.398(4) / 1.401 | -- / 1.403 | -- / 1.400 |
| C(15)–C(16) | 1.432(4) / 1.437 | 1.419(4) / 1.429 | -- / 1.425 | -- / 1.433 |
| C(16)–C(17) | 1.406(4) / 1.405 | 1.412(4) / 1.421 | -- / 1.428 | -- / 1.412 |
| C(17)–C(18) | 1.402(5) / 1.405 | 1.382(4) / 1.388 | -- / 1.386 | -- / 1.400 |
| C(18)–C(19) | 1.388(5) / 1.390 | 1.394(4) / 1.405 | -- / 1.406 | -- / 1.393 |
| C(19)–C(20) | 1.399(5) / 1.398 | 1.382(4) / 1.385 | -- / 1.381 | -- / 1.394 |
| C(20)–C(15) | 1.393(5) / 1.398 | 1.402(4) / 1.406 | -- / 1.406 | -- / 1.404 |



$^{a}$Crystals of **1** had two crystallographically unique but structurally similar molecules in the asymmetric unit. The bond distances shown here are for one molecule; the second molecule shows similar distances, see Supporting Information. $^{b}$Rh(1)–L = Rh–N(py). $^{c}$Rh(1)–L = Rh–PR$_3$.

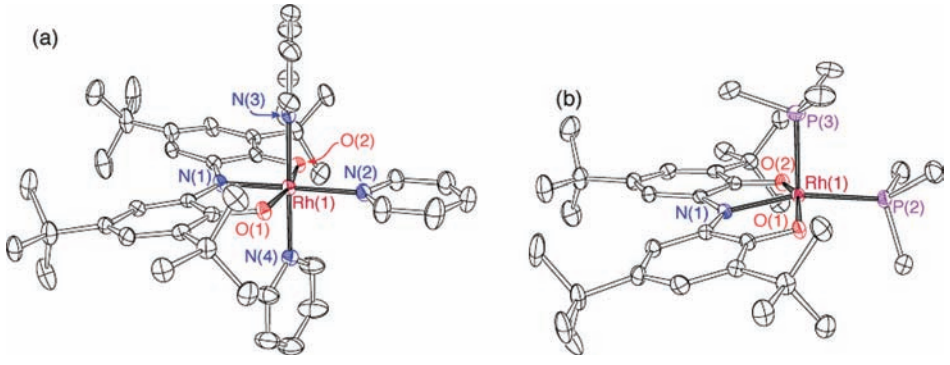


**Figure 2.** ORTEP diagrams of (a) [ONO$^{cat}$]Rh(py)$_3$ (**1**) and (b) [ONO]Rh(PMe$_3$)$_2$ (**2a**). Hydrogen atoms, solvent molecules, disorder, and a crystallographically unique but structurally analogous molecule of **1** have been omitted for clarity.

plane defined by the coordinating atoms of the basal plane. Complex **2a** manifests a short Rh–P bond for the apical phosphine ligand relative to the Rh–P bond for the phosphine in the basal plane. The Rh–P bonds in **2a** are generally shorter


dx.doi.org/10.1021/ic2026076 | *Inorg. Chem.* 2012, 51, 12606–12618

than those in octahedral $Rh^{III}$ complexes containing $PMe_3$ ligands,[68−70] but longer than the $Rh^{I}$−P bonds in the square planar complex $(PEt_3)_3Rh[O\text{-}(p\text{-tolyl})]$.[71]

Intraligand distances within the [ONO] platform are often used as a diagnostic tool for determining the ligand oxidation state since the $\pi$ bond order differs slightly for each of the ligand oxidation states shown in Scheme 1. Both **1** and **2a** exhibited C−O and C−N bond distances 0.03−0.10 Å longer than in the previously characterized $M[ONO^{q}]_2$ complexes (M = Zn, Ni, Pb) in which the [ONO] platform is fully oxidized,[21−23] and are more consistent with bond distances in formally reduced $\{[ONO^{cat}]M^{V}\}$ complexes.[18,28,29] The C(1)−C(2) and C(15)−C(16) bonds are often the longest aryl C−C bonds in [ONO] complexes regardless of coordinated metal and ligand oxidation state;[21,22,29] in both **1** and **2a** these bonds measure 1.42−1.44 Å, intermediate between C−C bonds in fully reduced aryl rings and nonaromatic $sp^2$−$sp^2$ carbon atoms.[72] The other aryl C−C bond distances in **1** and **2a** fall in a narrow range of 1.38−1.40 Å, which is more consistent with the $[ONO^{cat}]^{3-}$ ligand oxidation state than the oxidized $[ONO^{sq\bullet}]^{2-}$ or $[ONO^{q}]^{-}$ forms.[21,22]

**NMR Spectroscopy.** The NMR spectrum of **1** is consistent with the solid-state structure described above. Complex **1** exhibited a symmetric [ONO] ligand environment with two aromatic and two *tert*-butyl resonances in the $^1H$ NMR spectrum. The $^1H$ NMR spectrum of **1** shows two unique pyridine ligands in a 2:1 ratio, consistent with the inequivalent pyridine environments in the X-ray structure. The protons of the pyridine *trans* to the [ONO] nitrogen are shifted downfield compared to the pyridine molecules *cis* to the [ONO] nitrogen. The pyridine resonances for **1** did not coalesce upon heating to 60 °C; however, the addition of excess $d_5$-pyridine to the NMR sample resulted in the immediate ($\tau$ < 30 s) loss of the resonances for coordinated pyridine and the appearance of the resonances associated with 3 equiv of free $h_5$-pyridine. Attempts to use selective inversion-pulse NMR experiments showed that the pyridine exchange rate is slower at 298 K than the relaxation time of the pyridine protons (about 1 s), precluding exact measurement of the pyridine exchange rate.

In contrast to **1**, the $^1H$ NMR spectra of **2a−d** indicate a fluxional coordination environment on the NMR time scale. The [ONO] ligands of **2a−d** are symmetric by $^1H$ NMR spectroscopy showing two aryl and two *tert*-butyl resonances in all cases except **2d**, for which there is coincidental overlap of the [ONO] *tert*-butyl resonances. The $^1H$ NMR spectra of **2a−d** also show equivalent phosphine environments even upon cooling the samples to −90 °C. These features suggest a $C_{2v}$ molecular geometry on the NMR time scale, which can be explained by fast exchange between apical and basal phosphine positions in solution. Accordingly, the $^{31}P\{^1H\}$ NMR spectra of **2a−d** all showed a single doublet resonance with a P−Rh coupling constant of about 138 Hz that was not affected by temperature. The $^{31}P\{^1H\}$ resonances for **2a−d** are shifted to higher frequency than those in square-planar $(PR_3)_3Rh^{I}(OAr)$ complexes, suggesting a more electron-poor rhodium center.[71,73,74] Across the series **2a−d**, the $^{31}P\{^1H\}$ resonance shifts downfield with the increasing number of electron-withdrawing aryl substituents on the phosphorus atom.

The addition of excess phosphine to solutions of **2a** or **2b** resulted in changes to the NMR spectra that are indicative of the formation of six-coordinate phosphine adducts $[ONO^{cat}]Rh(PR_3)_3$ ($PR_3$ = $PMe_3$, **3a**; $PR_3$ = $PMe_2Ph$, **3b**). The $^1H$ NMR spectrum of **2a** in toluene-$d_8$ in the presence of excess $PMe_3$ showed an upfield shift of the aryl [ONO] resonances, bringing them to within 0.2 ppm of those observed for **1**. At 298 K, the $^1H$ NMR spectrum of **2a** plus added phosphine showed a single $PMe_3$ resonance, indicating rapid exchange of free and coordinated phosphine; however, cooling the sample to 228 K slowed the exchange process so separate $^1H$ NMR resonances could be resolved, indicating the presence of two different coordinated phosphine ligands as well as free $PMe_3$. A similar phenomenon was observed in the $^{31}P\{^1H\}$ NMR spectra of **2a** and added $PMe_3$. At 298 K the phosphorus resonances for **2a** and added $PMe_3$ in toluene-$d_8$ are broadened into the baseline, but at 213 K, sharp signals for free $PMe_3$ and two different rhodium-bound phosphine ligand environments were resolved. Both coordinated phosphine ligands showed Rh−P and P−P couplings with a doublet of doublets signal at −10.34 ppm corresponding to two $PMe_3$ ligands cis to the [ONO] nitrogen and a doublet of triplets signal at 4.29 ppm corresponding to a single $PMe_3$ ligand trans to the [ONO] nitrogen. This NMR data is indicative of the formation of $[ONO^{cat}]Rh(PMe_3)_3$ (**3a**) from association of a third $PMe_3$ ligand to the rhodium center in **2a**. Rhodium phosphine complex **2b** behaved similarly to **2a**: addition of excess $PMe_2Ph$ to **2a** afforded $[ONO^{cat}]Rh(PMe_2Ph)_3$ (**3b**). Derivatives **2c** and **2d** showed no NMR evidence for the formation of six-coordinate adducts upon addition of excess $PMePh_2$ and $PPh_3$, respectively.

**Electronic Spectroscopy.** The UV−visible spectra for **1** and **2a−d** showed distinctly different electronic structures for the six-coordinate pyridine adduct and the five-coordinate phosphine adducts. Figure 3 shows the electronic absorption

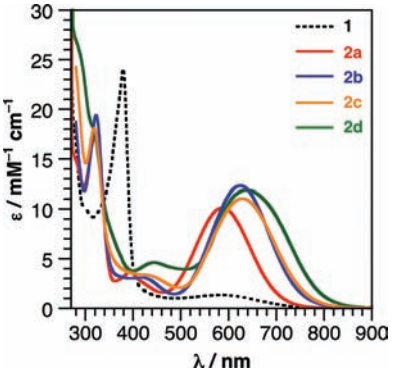


**Figure 3.** UV−vis absorption spectra of $[ONO^{cat}]Rh(py)_3$ (**1**), $[ONO]Rh(PMe_3)_2$ (**2a**), $[ONO]Rh(PMe_2Ph)_2$ (**2b**), $[ONO]Rh(PMePh_2)_2$ (**2c**), and $[ONO]Rh(PPh_3)_2$ (**2d**), acquired in $C_6H_6$ at 298 K.

spectra of **1** and **2a−d** collected at 298 K in benzene. The spectrum of **1** is dominated by a strong absorption band in the near-UV region at 380 nm along with a relatively weak, broad feature in the visible range. In comparison, the UV transitions in **2a−d** are blue-shifted by 60 nm compared to the UV transition in **1**, and a broad, intense, visible-region absorption band dominates the spectra between 530 and 630 nm. These visible absorption bands are responsible for the blue-green colors of **2a−d**, and are blue-shifted significantly from the ligand-based $\pi \rightarrow \pi^*$ transition of $[ONO^{q}]K$ discussed above.[15,20,22] Spectral features in the near-IR


dx.doi.org/10.1021/ic2026076 | Inorg. Chem. 2012, 51, 12606−12618

portion of the UV−vis spectrum ($\lambda_{max}$ > 900) are often observed in metal complexes containing the semiquinonate form of the ligand, $[ONO^{sq}]^{2-}$, but were not observed in the spectra of **1** or **2a**−**d**.[16,21,22] The broad visible transitions in **2a**−**d** are similar to the metal-to-ligand charge-transfer (MLCT) transitions observed in rhodium complexes containing $\pi$-acceptor ligands such as bipyridine, phenanthroline, and other $\alpha$-diimines,[42,66,75,76] in which the charge transfer character stems from interactions between filled metal d orbitals and antibonding ligand $\pi^*$ orbitals.

**Phosphine Binding Studies.** The conversion of **2a** and **2b** to **3a** and **3b**, respectively, by the addition of phosphine is readily evident in the electronic absorption spectra of these complexes, providing a reliable method for studying the thermodynamics associated with coordination of the third phosphine ligand. The addition of excess $PMe_3$ to **2a** or $PMe_2Ph$ to **2b** resulted in color changes from blue to brown/black. The brown/black color of **3a** and **3b** reverted to the blue color of **2a** and **2b**, respectively, upon dilution. Similarly, concentrating solutions of **3a** under vacuum resulted in reversion to the blue color of **2a**, attributable to the removal of volatile $PMe_3$. These results indicated coordination of a third phosphine ligand to **2a** and **2b** is reversible and concentration dependent. In the case of **2c** and **2d**, the addition of excess $PMePh_2$ and $PPh_3$, respectively, to solutions of the complexes did not result in an observable color change, consistent with the $^1$H NMR behavior reported above.

Equilibrium binding constants for the addition of phosphine to **2a** and **2b** were obtained from spectrophotometric titrations. As shown in Figure 4a, the addition of $PMe_3$ to a benzene solution of **2a** resulted in bleaching of the absorption bands at 321 and 587 nm with concomitant growth of a band at 393 nm. At concentrations of 40−50 $\mu$M of **2a** in benzene, approximately 160 equiv of $PMe_3$ were required to drive the formation of **3a** to completion. Similar results were obtained for titrations of **2b** with $PMe_2Ph$ as shown in Figure 4b, though solutions with a concentration of 40−50 $\mu$M in **2b** required approximately 1600 equiv of $PMe_2Ph$ to reach the end point. Analysis of the spectral data shown in Figure 4 using Hyperquad2003[54,55] gave log $K_{eq}$ = 3.77(3) for the addition of $PMe_3$ to **2a** ($\Delta G_{298K}$ = −5.14(4) kcal mol$^{-1}$) and log $K_{eq}$ = 2.01(2) for the addition of $PMe_2Ph$ to **2b** ($\Delta G_{298K}$ = −2.74(2) kcal mol$^{-1}$).

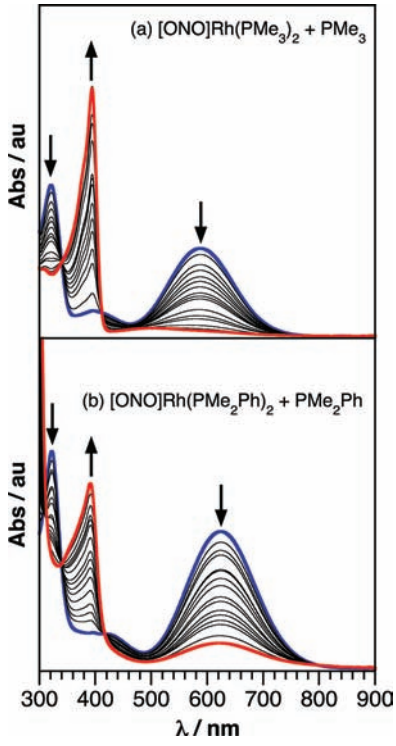


**Figure 4.** UV−visible absorption spectra for the titrations of (a) $[ONO]Rh(PMe_3)_2$ (**2a**) with 160 equiv of $PMe_3$ and (b) $[ONO]Rh(PMe_2Ph)_2$ (**2b**) with 1,600 equiv of $PMe_2Ph$. Titrations were conducted in $C_6H_6$ at 298 K.

Deconvolution of the end-point spectra for the titrations of **2a** and **2b** with phosphine using Hyperquad2003[54,55] provided calculated electronic absorption spectra for the tris(phosphine) adducts **3a** and **3b**. Figure 5 shows the calculated absorption spectra for **3a** and **3b**, which are strikingly similar to the absorption spectrum of **1**. Specifically, they exhibit a weak, broad absorbance across most of the visible region, a strong UV absorbance at about 390 nm, which is only 10 nm red-shifted from the similar feature in **1**. The similarity between the absorption spectra of **1**, **3a**, and **3b** and the strong differences between the spectra for these complexes and the spectra for **2a**−**d** indicates that the electronic structure of these [ONO]Rh complexes is very sensitive to the number of ligands coordinated to the metal center, though not necessarily to the type of ligand coordinated to the metal center.

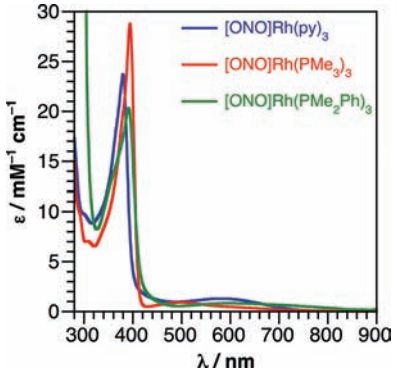


**Figure 5.** Comparison of the UV−vis absorption spectrum of $[ONO^{cat}]Rh(py)_3$ (**1**) with the calculated spectra for $[ONO^{cat}]Rh(PMe_3)_3$ (**3a**) and $[ONO^{cat}]Rh(PMe_2Ph)_3$ (**3b**). Spectra are in $C_6H_6$ at 298 K.

**Ligand Displacement Studies.** The relative energies of pyridine adduct **1** and phosphine adducts **2a**−**d** were probed by titration experiments. The conversion of solutions of $[ONO^{cat}]Rh(py)_3$ (**1**) to solutions of $[ONO]Rh(PPh_3)_2$ (**2d**) could be effected by the addition of $PPh_3$. Similar conversions were observed for the other phosphines. To avoid the complications associated with a second equilibrium between the bis- and tris(phosphine) derivatives, only the conversion between **1** and **2d** was studied in detail since there is no evidence for the formation of a $[ONO^{cat}]Rh(PPh_3)_3$ complex. Addition of at least 2 equiv of $PPh_3$ to a brown sample of **1** in $C_6D_6$ resulted in a blue/green solution whose $^1$H NMR spectrum was consistent with **2d** and free pyridine. When $[ONO^{cat}]Rh(py)_3$ (**1**) was titrated with $PPh_3$ using short equilibration times (2−4 h), a green solution was obtained for the addition of up to 1 equiv of phosphine.


dx.doi.org/10.1021/ic2026076 | Inorg. Chem. 2012, 51, 12606−12618

As the amount of phosphine increased above 1 equiv, the solution color became bluer. Figure 6a shows this result

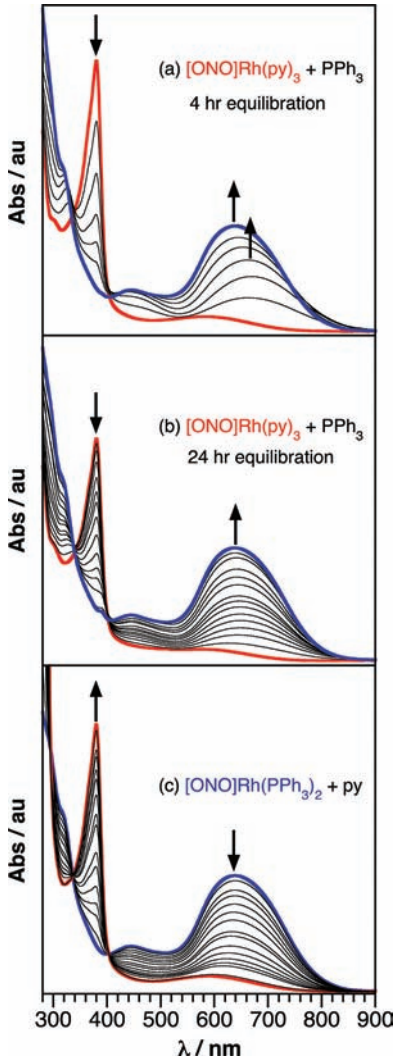


**Figure 6.** UV−visible absorption spectra for the titration of (a) **1** (ca. 50 $\mu$M) with $PPh_3$ (~2 equiv at end point) using a 2 h equilibration time, (b) **1** (ca. 50 $\mu$M) with $PPh_3$ (~2 equiv at end point) using a 4 day equilibration time, and (c) **2d** (ca. 50 $\mu$M) with pyridine (~2300 equiv at end point) using a 36 h equilibration time. All titrations were carried out in benzene at 298 K.

spectrophotometrically: for samples with up to 1 equiv of phosphine an absorption band grows in at 665 nm, but as the amount of phosphine increases above 1 equiv, this band blue-shifts to 640 nm. This result suggests the formation of an intermediate species, presumably [ONO]Rh(py)($PPh_3$) (eq 2), which then converts to **2d** upon addition of more $PPh_3$ (eq 3).

The putative, green, phosphine-pyridine intermediate, [ONO]Rh(py)($PPh_3$), is only metastable and disproportionates to **1** and **2d** at longer equilibration times. Figure 6b shows the UV−vis absorption spectra for a titration of $[ONO^{cat}]Rh(py)_3$ (**1**) with $PPh_3$ using a long equilibration time for each sample (24 h). No intermediate green species is observed when employing a long equilibration time, indicating that the putative [ONO]Rh(py)($PPh_3$) intermediate disproportionates to **1** and **2d** in the presence of pyridine (eq 4). To observe the intermediate species evident in Figure 6a, the disproportionation of eq 4 must be slow relative to the ligand displacement reactions of eq 2 and 3.

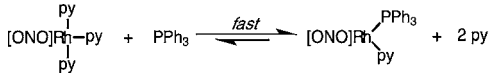


(2)

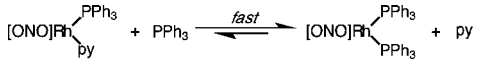


(3)

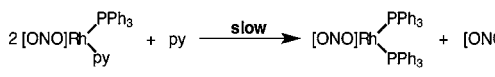


(4)

The ligand exchange reactions of eqs 2 and 3 are reversible as the triphenylphosphine ligands of **2d** could be replaced by pyridine to afford **1**, provided a large excess of pyridine is employed. The addition of excess pyridine-$d_5$ (ca. 5000 equiv) to a solution of **2d** in $C_6D_6$ gave a $^1H$ NMR spectrum consistent with the formation of **1** and liberated $PPh_3$. When this reaction was carried out as a spectrophotometric titration (low concentrations are required for phosphine dissociation to go to completion), the UV−vis spectra shown in Figure 6c were obtained, showing clean conversion of **2d** to **1** with no evidence of a long-lived intermediate. An overall equilibrium constant, $K_{disp} = 4.6(7) \times 10^{-4}$, was extracted from the plot in Figure 6c corresponding to a free energy change $\Delta G_{298} = 4.55 \pm 0.10$ kcal mol$^{-1}$ for eq 5.

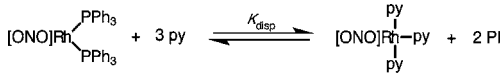


(5)

**Phosphine Exchange Studies.** In addition to the association of phosphine ligands to five-coordinate complexes **2a** and **2b**, these complexes undergo a pseudo self-exchange or comproportionation of the coordinated phosphine ligands. Complexes **2a** and **2b** in $C_6D_6$ solution at room temperature reacted to afford the mixed phosphine complex [ONO]Rh-($PMe_3$)($PMe_2Ph$) (**4**). Complex **4** was identified by a new set of [ONO] ligand resonances in the $^1H$ NMR spectrum along with two new phosphine resonances in the $^{31}P\{^1H\}$ NMR spectrum (see Supporting Information). ESI mass spectrometry confirmed the formation of **4** with the parent ion ($M^+$) peak observed at 739.2 amu. The formation of **4** is an equilibrium exchange process that proceeds without an observable color change, but that can be monitored by $^{31}P\{^1H\}$ NMR spectroscopy. By NMR integration measurement, the equilibrium constant ($K_{com}$) at 298 K for eq 6 was determined to be 12.5(3), corresponding to a free energy change of −1.50(2) kcal mol$^{-1}$.

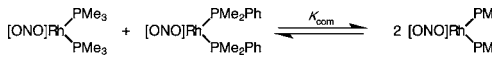


(6)

**Electrochemistry.** Cyclic voltammetric measurements were conducted on **1** and **2a**−**d** to probe their redox behavior. Figure 7 shows the CV traces for each complex; redox potentials are summarized in Table 3. All potentials are referenced to the $[Cp_2Fe]^{+/0}$ couple. The CVs of **2a**−**d** were insensitive to the presence of excess phosphine ligand. Each complex shows two reversible, one-electron oxidation processes. The first oxidation process is strongly dependent on the nature of the ancillary ligand. The first oxidation of tris(pyridine) complex **1**, $\{[ONO]Rh(py)_3\}^{+/0}$, is observed at −0.91 V whereas the first oxidation of bis(triphenylphosphine) complex **2d** is shifted 640 mV more positive to −0.27 V. The first oxidation events for **2a**−**c** fall in the region −0.60 to −0.69 V, approximately


dx.doi.org/10.1021/ic2026076 | Inorg. Chem. 2012, 51, 12606−12618

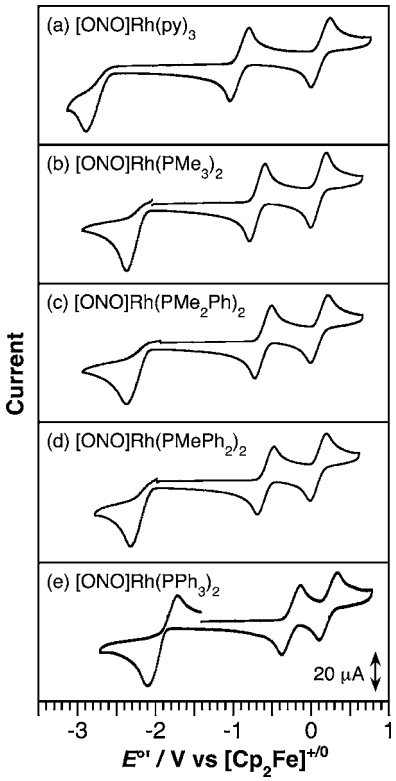


**Figure 7.** Cyclic voltammograms of **1** and **2a**–**2d**. Spectra were recorded at 1 mM analyte concentration in 0.1 M $[NBu_4][PF_6]$ in dry, degassed THF under a nitrogen atmosphere using a 3 mm glassy carbon working electrode, Pt counter electrode, and silver wire reference electrode, at 300 K with a 200 mV/s scan rate.

**Table 3. Reduction Potentials vs. $[FeCp_2]^{+/0}$ of $[ONO]RhL_n$ Complexes**[a]

| | $E°'$/V vs $[Cp_2Fe]^{1+/0}$ | | |
|---|---|---|---|
| | $\{[ONO]RhL_n\}^{2+/1+}$ | $\{[ONO]RhL_n\}^{1+/0}$ | $\{[ONO]RhL_n\}^{0/2-}$ |
| **1** | 0.12(1) [0.98] | −0.91(1) [1.03] | −2.87(2)[b] |
| **2a** | 0.10(1) [1.01] | −0.69(1) [1.06] | −2.40(3)[b] |
| **2b** | 0.10(1) [1.01] | −0.60(1) [1.03] | −2.32(4)[b] |
| **2c** | 0.07(3) [1.02] | −0.61(3) [1.09] | −2.34(3)[b] |
| **2d** | 0.19(2) [1.06][c] | −0.27(1) [1.06] | −2.11(3)[b] [1.90][c] |

[a]Conditions are detailed in Figure 7. Bracketed values are $i_{pa}/i_{pc}$ ratios at 200 mV $sec^{-1}$. [b]Irreversible, $2e^-$ process ($E_{pc}$). [c]$i_{pc}/i_{pa}$ at 200 mV $sec^{-1}$.

halfway between those of **1** and **2d**. The second oxidation process, $\{[ONO]RhL_n\}^{2+/+}$ is insensitive both to the rhodium coordination geometry and to the ancillary ligands with the potentials for **1** and **2a**–**d** falling in the narrow window +0.07 to +0.19 V. Reduction of **1** and **2a**–**d** occurred in an irreversible two-electron process (as determined by peak integration) that again was dependent on the ancillary ligand. Triphenylphosphine derivative **2d** was reduced most easily at −2.11 V while tris(pyridine) complex **1** required −2.87 V to drive the reduction. As with the first oxidation potential, the reduction potentials of complexes **2a**–**c** fell in between those for **1** and **2d**. The two-electron reductions of **1** and **2a**–**c** appear completely irreversible at 200 mV $sec^{-1}$, and while the reduction of **2d** appears to be at least partially reversible, the $i_{pc}/i_{pa}$ ratio for this reduction was found to be independent of scan rate, indicating a partially irreversible process.

**DFT Calculations.** The electronic structural properties of **1**, **2a**, **2d**, and **3a** were examined by DFT computations. Calculations were carried out without symmetry constraints at the B3LYP/TZVP level of theory. For complexes **1** and **2a**, the coordinates from the single-crystal X-ray diffraction structures were used as a starting point for the geometry optimizations. The starting structure for the optimization of $[ONO^{cat}]Rh(PMe_3)_3$ (**3a**) was generated by replacing the three pyridine ligands of **1** with three $PMe_3$ ligands. The ground state solution for all four complexes proved to be the closed-shell singlet state ($S = 0$), consistent with the diamagnetic character of **1**, **2a**, **2d**, and **3a**. Attempts to locate an open-shell singlet (i.e., a broken-symmetry singlet) resulted in collapse of the calculation to the closed-shell solution. The triplet ($S = 1$ spin system) energies for **1**, **2a**, and **3a** were found to lie several kcal $mol^{-1}$ above the $S = 0$ state. The optimized geometries of both **1** and **2a** were similar to the crystal structures, and pertinent bond distances are listed in Table 2. The largest discrepancies in the bond lengths between crystallographic and calculated structures is the 0.06 Å difference in the Rh(1)–P(2) distance, but most bonds varied by less than 0.03 Å. The structure of **3a** minimized to a distorted octahedral coordination geometry similar to that of **1**; selected bond distances for this solution are shown in Table 2. The calculated structure of **2d** minimized to a coordination geometry of a slightly distorted trigonal bipyramid (see Supporting Information). This assignment is borne out by the calculated equatorial bond angles in the calculated structure of **2d**, in which $N_{ONO}$–Rh–P angles are 138° and 119°, with a P–Rh–P angle of 103°; in comparison, measured $N_{ONO}$–Rh–P angles in **2a** were 155° and 106° with a P–Rh–P bond angle of 96°. The relaxation of **2d** toward trigonal bipyramidal geometry presumably is driven by the increased steric bulk of the $PPh_3$ ligands. Notably, the aryl C–C bond distances within the [ONO] ligands (excepting C(1)–C(2) and C(15)–C(16)) of **1**, **2a**, **2d**, and **3a**, were all calculated to be 1.40 ± 0.02 Å, strongly indicative of a $[ONO^{cat}]^{3-}$ oxidation state of the redox-active ligand across all four complexes.

An analysis of the frontier molecular orbitals of **1**, **2a**, and **3a** provide insight into the electronic differences between the five- and six-coordinate $[ONO]RhL_n$ complexes. Figure 8 shows calculated frontier molecular orbital diagrams for each complex. Orbitals of principally d character are labeled accordingly, with the [ONO] ligand oriented in the xy plane. The relative orbital energies and overall appearance of the frontier molecular orbitals in **1** and **3a** are similar, and follow the expected pattern for a $d^6$ octahedral complex. The highest occupied molecular orbital (HOMO) and HOMO−1 correspond to the Rh($d_{yz}$)–$N_{ONO}$($p_z$) and Rh($d_{xz}$)–$O_{ONO}$($p_z$) $\pi^*$ orbitals, respectively, and are localized mainly on the [ONO] ligand. The $t_{2g}$-like metal orbitals $d_{xy}$, $d_{xz}$, and $d_{yz}$ are lower in energy and filled. As expected for an octahedral complex, the metal $d_{z^2}$ and $d_{x^2-y^2}$ orbitals are $\sigma$-antibonding with respect to the ligand set. In the case of **3a** the $d_{z^2}$ orbital is the LUMO of the complex and the $d_{x^2-y^2}$ is the LUMO+1. In the case of **1**, the $\pi^*$ orbitals of the pyridine ligands fall below the metal $d_{z^2}$ and $d_{x^2-y^2}$ orbitals; however, the metal orbitals maintain the same energy ordering as in **3a**.

The relative energies and appearance of the frontier orbitals in **2a** (Figure 8) and **2d** (see Supporting Information) are significantly different from the orbitals of **1** and **3a**. Notably, the HOMO and lowest unoccupied molecular orbital (LUMO) of **2a** both contain significant rhodium $d_{z^2}$ character. The distorted


dx.doi.org/10.1021/ic2026076 | Inorg. Chem. 2012, 51, 12606–12618

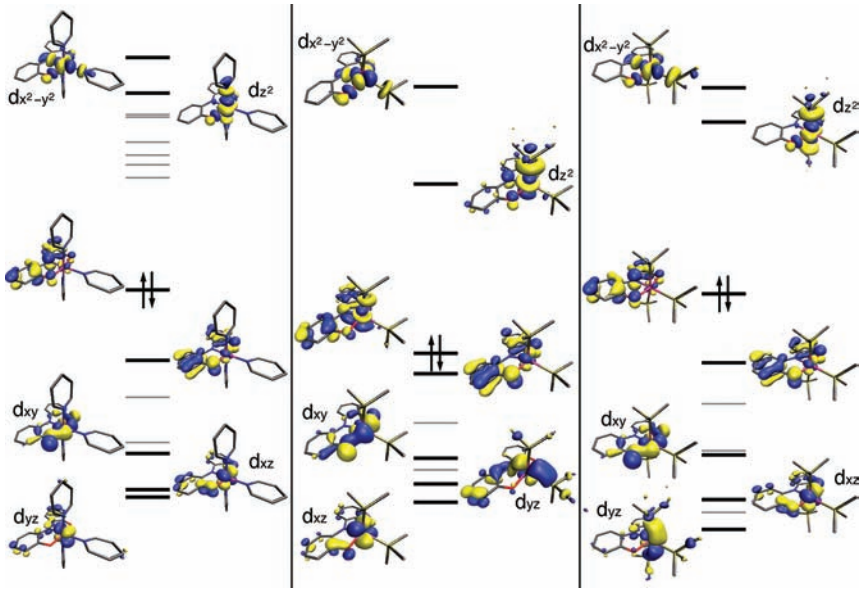


**Figure 8.** Calculated frontier molecular orbital diagrams displaying Kohn–Sham orbitals for **1** (left), **2a** (center), and **3a** (right). For each compound, the HOMO is designated with an electron pair. For clarity, only the HOMO, HOMO-1, and primarily d-based orbitals are illustrated.

square pyramidal geometry of **2a** places the rhodium atom 0.28 Å above the mean-squared plane defined by the coordinating atoms of the [ONO] ligand and P(1). Because of this distortion, the rhodium $d_{z^2}$ has a nonzero overlap with the highest-energy filled $\pi$ orbital of the [ONO] ligand, creating a filled Rh–N $\pi$ orbital and an empty Rh–N $\pi^*$ orbital. A similar $\pi$ bonding interaction exists in **2d**, with the caveat that the d-orbital hybridization changes slightly owing to the change between square-pyramidal and trigonal bipyramidal geometries.

Natural population analysis was performed on the calculated structures of **2a**, **2d**, and **3a** to better quantify the localization of the HOMO and LUMO in these representative structures. The results of these calculations are listed in Table 4, with a more detailed table in the Supporting Information. As the molecular orbitals in Figure 8 suggest, 90% of the HOMO of the octahedral **3a** resides on the [ONO] ligand, with only 3% rhodium character in the HOMO, supporting a formal $[ONO^{cat}]Rh^{III}L_3$ electronic configuration. In **2a** and **2d**, however, the [ONO] contribution to the HOMO decreases to approximately 60% with the rhodium contribution to the HOMO increasing to 27%, indicating a more reduced rhodium metal center in **2a** and **2d** compared to **3a**.

**Table 4. Natural Population Analysis Orbital Contributions in [ONO]RhL$_n$ Complexes in Number of Electrons (percent)**

| | 2a | | 2d | | 3a | |
|---|---|---|---|---|---|---|
| | HOMO | LUMO | HOMO | LUMO | HOMO | LUMO |
| Rh | 0.53 (27%) | 0.79 (40%) | 0.54 (27%) | 0.66 (33%) | 0.06 (3%) | 1.10 (55%) |
| [ONO] | 1.28 (64%) | 0.76 (38%) | 1.20 (60%) | 0.86 (43%) | 1.80 (90%) | 0.31 (16%) |

## DISCUSSION

**Electronic Structure.** Both the [ONO] ligand and rhodium metal can exist in multiple oxidation states, allowing for three plausible electron distributions for [ONO]Rh complexes **1**–**3**: $[ONO^{cat}]Rh^{III}$, $[ONO^{sq\bullet}]Rh^{II}$, and $[ONO^{q}]Rh^{I}$. Experimental evidence showed that complexes **1**–**3** exist as $S$ = 0 complexes with no unpaired electrons. In the case of $[ONO^{cat}]Rh^{III}$ and $[ONO^{q}]Rh^{I}$ electron distributions, closed-shell electron configurations on both the ligand and the metal would give rise to an overall $S$ = 0 spin state. For a $[ONO^{sq}]Rh^{II}$ electron configuration, two qualitative descriptions are possible. The first possibility is an open-shell biradical configuration with antiferromagnetic coupling between the unpaired metal and ligand electrons to give an $S$ = 0 spin state as has been observed for other rhodium complexes with redox-active ligands.[38] DFT computations on **1**–**3** do not support this open-shell, singlet-diradical electron configuration. Consistent with these results, all attempts to calculate a "broken-symmetry" singlet electronic configuration resulted in collapse of the calculation to a closed-shell, $S$ = 0 solution; furthermore, the absence of low-energy ($\lambda_{max}$ > 900 nm), intraligand $\pi \rightarrow \pi^*$ transitions typical of the semiquinonate $[ONO^{sq}]^{2-}$ ligand[19–22] further refute the existence of open-shell, singlet-diradical character in **1**–**3**. The second qualitative description that would give rise to a $[ONO^{sq}]Rh^{II}$ electron configuration would be to pair up the odd $[ONO^{sq}]^{2-}$ electron and the odd $Rh^{II}$ electron in a shared molecular orbital such as a $\pi$ bond to afford an $S$ = 0 spin state, consistent with the experimental evidence for **1**–**3**.

Structural metrics and spectroscopic properties of the six-coordinate rhodium complexes are consistent with their assignment as $[ONO^{cat}]Rh^{III}$ complexes. The six-coordinate, pseudo-octahedral structure of **1** is completely consistent with its assignment as a rhodium(III) complex. Bond metrics within the [ONO] ligand support this contention, specifically with C–C ring distances in the range of 1.39–1.44 Å and single-bond C–N and C–O distances. Spectroscopically, complex **1** shows only weak absorptions in the visible region accompanied by a strong charge-transfer absorption at 380 nm. The $^1$H NMR spectrum of **1** shows two distinct pyridine environments, consistent with a meridional arrangement of three pyridine ligands and slow ligand exchange as expected for a $d^6$ octahedral complex of rhodium. These data indicate that $[ONO^{cat}]Rh^{III}(py)_3$ is both the best *formal* and *spectroscopic* oxidation state assignment for **1**, an assignment that is supported by DFT


dx.doi.org/10.1021/ic2026076 | *Inorg. Chem.* 2012, 51, 12606–12618

calculations. The strong correlation between the UV−vis absorption spectra of **1** and **3a**−**b** support the assignment of **3a** and **3b** as $[ONO^{cat}]Rh^{III}(PMe_3)_3$ and $[ONO^{cat}]Rh^{III}(PMe_2Ph)_3$, respectively, a conclusion that is also supported by DFT results.

The striking UV−vis absorption spectra of **2a**−**d** suggested a different electronic configuration for these five-coordinate complexes relative to the six-coordinate complexes **1** and **3a**−**b**. Isolated phosphine adducts of the [ONO]Rh core in the solid state contained only two phosphine ligands to give five-coordinate $[ONO]RhL_2$ complexes. There is no direct evidence for four-coordinate, [ONO]RhL derivatives, which is surprising given the proclivity for rhodium to adopt a square-planar geometry and a $d^8$ electron configuration; even with very bulky phosphines, a stable four-coordinate $[ONO]Rh(PR_3)$ complex was never successfully isolated. Complexes **2a**−**d** show strong UV−vis absorptions in the visible region of the spectrum with maxima in the range of 530−630 nm. Such absorptions are reminiscent of the absorption features of rhodium(I) complexes such as the $[Rh(bpy)_2]^+$ cation,[77,78] which has an MLCT absorbance at 556 nm, suggesting a possible oxidation state assignment of $[ONO^q]Rh^IL_2$ for complexes **2a**−**d**. Conversely, the intraligand bond metrics in the X-ray structure of **2a** are not consistent with an $[ONO^q]^-$ ligand oxidation state. Specifically, the C−C ring distances vary by only 0.03 Å, whereas $[ONO^q]^-$ ligands typically have C−C bond distances that vary by 0.10 Å,[21−23] indicative of a cyclohexadiene ring. Thus, the experimental data does not support a $[ONO^q]Rh^I$ electronic configuration in **2a** (and by analogy in **2b**−**2d**).

The electronic configuration of **2a**−**d** is further muddled upon consideration of the electrochemical data for complexes **1** and **2a**−**d**. All five complexes show the same number of redox processes in the electrochemical window between −3 V and +1 V. Complex **1** is the easiest to oxidize and the hardest complex to reduce, while complex **2d**, with the bulky $PPh_3$ ligand, is the hardest to oxidize and the easiest to reduce. Both the oxidations and the reductions of complexes **2a**−**c** lie in between the extremes represented by **1** and **2d**. The consistent trend in redox properties among the five complexes argues against an abrupt change in electronic structure between **1** and **2a**−**d**. Furthermore, since the electrochemical data acquired for **2a**−**d** is the same in the absence and in the presence of excess phosphine, the formation of six-coordinate adducts **3a** and **3b** do not perturb the overall electronic structure of these complexes significantly

The electronic difference between five- and six-coordinate [ONO]Rh complexes was best illustrated in the DFT calculations. In the case of pseudo-octahedral complexes **1** and **3a**, DFT calculations afforded a frontier orbital picture consistent with the expected $d^6$ $Rh^{III}$ configuration. The rhodium $d_{xy}$, $d_{xz}$, and $d_{yz}$ orbitals are fully occupied (Figure 8) while the $d_{z^2}$ and $d_{x^2-y^2}$ orbitals are empty and displaced to higher energy owing to their $\sigma^*$ parentage with respect to the ligand field. The calculated HOMOs for **1** and **3a** are [ONO]-ligand-centered $\pi^*$ orbitals. In the case of **1**, the LUMO is based on the coordinated pyridine ligands; for **3a**, the LUMO is the rhodium $d_{z^2}$ orbital. In the cases of **1** and **3a**−**b**, the regular octahedral geometry of these complexes confers classical coordination complex electronic behavior and these complexes are well described as $[ONO^{cat}]Rh^{III}L_3$ species.

The distorted five-coordinate geometry of **2a** results in a different frontier orbital configuration. While the rhodium $d_{xy}$, $d_{xz}$, and $d_{yz}$ orbitals are fully occupied and the $d_{x^2-y^2}$ orbital is an empty $\sigma^*$ orbital, Figure 8 shows that both the calculated HOMO and LUMO of **2a** have significant metal $d_{z^2}$ parentage. The distorted square-pyramidal geometry of **2a** results in an obtuse angle (100°) between the apical phosphine donor, the rhodium center, and the [ONO] nitrogen and bestows nonzero overlap between the rhodium $d_{z^2}$ orbital and the highest energy [ONO]-ligand $\pi^*$ orbital. These two orbitals interact as illustrated in Figure 8 to form Rh−[ONO] $\pi$ and $\pi^*$ combinations that constitute the HOMO and LUMO, respectively, of the complex. Thus, the strong, low-energy absorption observed in the UV−vis spectrum of **2a** can be assigned as a HOMO−LUMO, $\pi$ to $\pi^*$ transition. DFT calculations of the calculated structure for **2d** revealed similar Rh−[ONO] $\pi$ and $\pi^*$ interactions in the HOMO and LUMO, respectively.

Five-coordinate rhodium complexes **2a**−**d** are best described as having *experimental* oxidation states that lie between $[ONO^{sq}]Rh^{II}(PR_3)_2$ and $[ONO^{cat}]Rh^{III}(PR_3)_2$. As shown in Figure 8 and in the Supporting Information, the HOMO electron pair in **2a** and **2d** (and by analogy, **2b** and **2c**) is shared between the rhodium center and the [ONO] ligand in a $\pi$-bonding orbital. The sharing of this electron pair between the rhodium center and the [ONO] ligand leads to the distinct electronic character of complexes **2a**−**d**, while the polarization of the $\pi$ bond toward the [ONO] ligand suggests an electron distribution between $[ONO^{sq}]Rh^{II}(PR_3)_2$ and $[ONO^{cat}]$-$Rh^{III}(PR_3)_2$. The proclivity for **2a** and **2b** to add reversibly a third phosphine ligand is consistent with an experimental oxidation state between $[ONO^{sq}]Rh^{II}(PR_3)_2$ and $[ONO^{cat}]$-$Rh^{III}(PR_3)_2$, since a five-coordinate rhodium(III) complex would be expected to be Lewis acidic. Incidentally, population analysis of **2d** revealed similar contributions from the [ONO] ligand and the rhodium center to the HOMO and LUMO, supporting the argument that association of a third phosphine ligand ligand to **2c** and **2d** is inhibited by steric rather than electronic considerations.

**Ligand Exchange Reactions.** Ligand exchange studies of the $[ONO]RhL_n$ complexes reveal a complicated energetic landscape with stable coordination geometries that are influenced by both the steric and the electronic properties of the auxiliary ligand. In the case of **1**, with pyridine donor ligands, only the six-coordinate geometry was observed; however, the pyridine ligands of **1** are labile and can be readily substituted in solution. Considering that **1** is a $d^6$, pseudo-octahedral complex, ligand exchange likely occurs through a dissociative pathway; this suggests that a five-coordinate intermediate, $[ONO]Rh(py)_2$, is energetically accessible under mild conditions. Consistent with this proposal, degenerate pyridine exchange occurs on a time scale of seconds and replacement of the pyridine ligands of **1** with stronger $\sigma$-donor phosphines such as $PMe_3$ or $PMe_2Ph$, rapidly affords both five and six-coordinate phosphine adducts. Titration experiments indicated an overall thermodynamic stability in which the tris(phosphine) complexes **3a** and **3b** are favored over bis-(phosphine) complexes **2a**−**d**, which are favored over tris-(pyridine) complex **1a**; however, the presence of a large excess of phosphine is required to push the formation of **3a** and **3b** to completion at low concentrations. The favorability of the six-coordinate phosphine complexes is likely driven by electronic considerations, with coordination of the sixth ligand quenching the Lewis acidic behavior of the rhodium $d_{z^2}$ orbital to form a traditional Werner-type coordination complex. The electronic preference for a pseudo-octahedral geometry is slight, though, since five-coordinate complexes are only observed for **2c** and **2d**, which employ the sterically demanding phosphine ligands $PMePh_2$ or $PPh_3$, respectively. In these two complexes, the energetic


dx.doi.org/10.1021/ic2026076 | *Inorg. Chem.* 2012, 51, 12606−12618

penalty for coordinating a third, sterically demanding phosphine ligand is not fully compensated by the quenching of the Lewis acidic rhodium $d_{z^2}$ orbital and formation of the third Rh−P bond. In the five-coordinate complexes **2a−d** the rhodium $d_{z^2}$ orbital is partially stabilized through $\pi$ bonding with the nitrogen donor of the $[ONO^{cat}]^{3-}$ ligand.

## CONCLUDING REMARKS

Care must be taken when describing the electronic structure of coordination complexes with redox-active or noninnocent ligands. In the case of complexes **2a−d**, a rigid view of formal metal and ligand oxidation states de-emphasizes the importance of covalency in the bonding between the rhodium and [ONO] ligand. This fact is readily apparent in complexes **2a−d**, in which both the [ONO] ligand and the rhodium metal center make significant contributions to the $\pi$-bonding HOMO and $\pi$-antibonding LUMO giving rise to unique spectroscopic properties. In these complexes, the *formal* oxidation state is $[ONO^{cat}]Rh^{III}(PR_3)_2$; however, it is better to consider $[ONO^{cat}]Rh^{III}(PR_3)_2$ and $[ONO^{sq}]Rh^{II}(PR_3)_2$ as limiting resonance structures for **2a−d** to emphasize that the HOMO electron pair is shared by both metal and ligand centers. It is important to note that the $[ONO^{sq}]Rh^{II}(PR_3)_2$ electron configuration proposed here, which arises from a covalent $\pi$-bonding interaction between the [ONO] ligand and the rhodium metal center, is distinct from an open-shell, singlet-biradical electron configuration.

The reversible coordination of a sixth ligand to **2a** and **2b** is intriguing because it results in a dramatic change to the spectroscopic properties of the rhodium complexes. That these spectroscopic changes can be contributed to a change in the rhodium $d_{z^2}$ orbital energy and a transfer of electron density from rhodium to the [ONO] ligand is reminiscent of similar coordination-induced electronic rearrangements in four-coordinate nickel salen and germanium porphyrin complexes.[79,80] In these examples, the four coordinate metal centers readily add two pyridine ligands to afford six-coordinate complexes which leads to the transfer of electron density away from the metal center and to the salen or porphyrin ligand.

## ASSOCIATED CONTENT

### Supporting Information

Crystallographic data refinement details and crystallographic information files for reported X-ray structures, supporting titration spectra, MO diagrams for **2d**, and $^{1}H$, $^{13}C\{^{1}H\}$, and $^{31}P\{^{1}H\}$ NMR spectra for all new complexes. This material is available free of charge via the Internet at http://pubs.acs.org.

## AUTHOR INFORMATION

### Corresponding Author

*E-mail: aheyduk@uci.edu.

### Notes

The authors declare no competing financial interest.

## ACKNOWLEDGMENTS

The authors thank the UCI Physical Science Center for Solar Energy for supporting this work. They also thank Dr. Philip Dennison for help with the NMR measurements. A.F.H. is a Camille Dreyfus Teacher-Scholar.

## REFERENCES

(1) Kaim, W.; Schwederski, B. *Coord. Chem. Rev.* **2010**, *254*, 1580−1588.
(2) Kaim, W.; Schwederski, B. *Pure Appl. Chem.* **2004**, *76*, 351−364.
(3) Kaim, W.; Lahiri, G. K. *Angew. Chem., Int. Ed.* **2007**, *46*, 1778−1796.
(4) Bart, S. C.; Chlopek, K.; Bill, E.; Bouwkamp, M. W.; Lobkovsky, E.; Neese, F.; Wieghardt, K.; Chirik, P. J. *J. Am. Chem. Soc.* **2006**, *128*, 13901−13912.
(5) Masui, H.; Lever, A. B. P.; Auburn, P. R. *Inorg. Chem.* **1991**, *30*, 2402−2410.
(6) Adams, D. M.; Noodleman, L.; Hendrickson, D. N. *Inorg. Chem.* **1997**, *36*, 3966−3984.
(7) Pierpont, C. G. *Coord. Chem. Rev.* **2001**, *219−221*, 415−433.
(8) Pierpont, C. G.; Buchanan, R. M. *Coord. Chem. Rev.* **1981**, *38*, 45−87.
(9) Chaudhuri, P.; Verani, C. N.; Bill, E.; Bothe, E.; Weyhermüller, T.; Wieghardt, K. *J. Am. Chem. Soc.* **2001**, *123*, 2213−2223.
(10) Zanello, P.; Corsini, M. *Coord. Chem. Rev.* **2006**, *250*, 2000−2022.
(11) Blackmore, K. J.; Lal, N.; Ziller, J. W.; Heyduk, A. F. *J. Am. Chem. Soc.* **2008**, *130*, 2728−2729.
(12) Vechorkin, O.; Csok, Z.; Scopelliti, R.; Hu, X. *Chem.—Eur. J.* **2009**, *15*, 3889−3899.
(13) Nguyen, A. I.; Blackmore, K. J.; Carter, S. M.; Zarkesh, R. A.; Heyduk, A. F. *J. Am. Chem. Soc.* **2009**, *131*, 3307−3316.
(14) Nguyen, A. I.; Zarkesh, R. A.; Lacy, D. C.; Thorson, M. K.; Heyduk, A. F. *Chem. Sci.* **2011**, *2*, 166−169.
(15) Girgis, A. Y.; Balch, A. L. *Inorg. Chem.* **1975**, *14*, 2724−2727.
(16) Camacho-Camacho, C.; Merino, G.; Martinez-Martinez, F. J.; Nöth, H.; Contreras, R. *Eur. J. Inorg. Chem.* **1999**, 1021−1027.
(17) Ohkata, K.; Yano, T.; Kuwaki, T.; Akiba, K. *Chem. Lett.* **1990**, *19*, 1721−1724.
(18) Poddel'sky, A. I.; Vavilina, N. N.; Somov, N. V.; Cherkasov, V. K.; Abakumov, G. A. *J. Organomet. Chem.* **2009**, *694*, 3462−3469.
(19) Evangelio, E.; Bonnet, M.-L.; Cabañas, M.; Nakano, M.; Sutter, J.-P.; Dei, A.; Robert, V.; Ruiz-Molina, D. *Chem.—Eur. J.* **2010**, *16*, 6666−6677.
(20) Caneschi, A.; Corina, A.; Dei, A. *Inorg. Chem.* **1998**, *37*, 3419−3421.
(21) Bruni, S.; Caneschi, A.; Cariati, F.; Delfs, C.; Dei, A.; Gatteschi, D. *J. Am. Chem. Soc.* **1994**, *116*, 1388−1394.
(22) Chaudhuri, P.; Hess, M.; Hildenbrand, K.; Bill, E.; Weyhermüller, T.; Wieghardt, K. *Inorg. Chem.* **1999**, *38*, 2781−2790.
(23) McGarvey, B. R.; Ozarowski, A.; Tian, Z.; Tuck, D. G. *Can. J. Chem.* **1995**, *73*, 1213−1222.
(24) Simpson, C. L.; Boone, S. R.; Pierpont, C. G. *Inorg. Chem.* **1989**, *28*, 4379−4385.
(25) Camacho-Camacho, C.; Tlahuext, H.; Nöth, H.; Contreras, R. *Heteroat. Chem.* **1998**, *9*, 321−326.
(26) Camacho-Camacho, C.; Mijangos, E.; Castillo-Ramos, M. E.; Esparza-Ruiz, A.; Vásquez-Badillo, A.; Nöth, H.; Flores-Parra, A.; Contreras, R. *J. Organomet. Chem.* **2010**, *695*, 833−840.
(27) Chaudhuri, P.; Hess, M.; Weyhermüller, T.; Wieghardt, K. *Angew. Chem., Int. Ed.* **1999**, *38*, 1095−1098.
(28) Zarkesh, R. A.; Heyduk, A. F. *Organometallics* **2009**, *28*, 6629−6631.
(29) Zarkesh, R. A.; Ziller, J. W.; Heyduk, A. F. *Angew. Chem., Int. Ed.* **2008**, *47*, 4715−4718.
(30) Zarkesh, R. A.; Heyduk, A. F. *Organometallics* **2011**, *30*, 4890−4898.
(31) Szigethy, G.; Heyduk, A. F. *Inorg. Chem.* **2011**, *50*, 125−135.
(32) Blackmore, K. J.; Lal, N.; Ziller, J. W.; Heyduk, A. F. *Eur. J. Inorg. Chem.* **2009**, 735−743.
(33) Blackmore, K. J.; Sly, M. B.; Haneline, M. R.; Ziller, J. W.; Heyduk, A. F. *Inorg. Chem.* **2008**, *47*, 10522−10532.
(34) Ketterer, N. A.; Fan, H.; Blackmore, K. J.; Yang, X.; Ziller, J. W.; Baik, M.-H.; Heyduk, A. F. *J. Am. Chem. Soc.* **2008**, *130*, 4364−4374.

(35) Haneline, M. R.; Heyduk, A. F. *J. Am. Chem. Soc.* **2006**, *128*, 8410−8411.
(36) Blackmore, K. J.; Ziller, J. W.; Heyduk, A. F. *Inorg. Chem.* **2005**, *44*, 5559−5561.
(37) Colby, D. A.; Bergman, R. G.; Ellman, J. A. *Chem. Rev.* **2010**, *110*, 624−655.
(38) DeWit, D. G. *Coord. Chem. Rev.* **1996**, *147*, 209−246.
(39) Huang, K.-W.; Han, J. H.; Musgrave, C. B.; Fujita, M. *Organometallics* **2007**, *26*, 508−513.
(40) Schwartzburd, L.; Iron, M. A.; Konstantinovski, L.; Ben-Ari, E.; Milstein, D. *Organometallics* **2011**, *30*, 2721−2729.
(41) Albert, G.; Berg, C.; Beyer, M.; Achatz, U.; Joos, S.; Niedner-Schatteburg, G.; Bondybey, V. E. *Chem. Phys. Lett.* **1997**, *268*, 235−241.
(42) Shaffer, D. W.; Ryken, S. A.; Zarkesh, R. A.; Heyduk, A. F. *Inorg. Chem.* **2011**, *50*, 13−21.
(43) Allgeier, A. M.; Mirkin, C. A. *Angew. Chem., Int. Ed.* **1998**, *37*, 895−908.
(44) van der Vlugt, J. I.; Reek, J. N. H. *Angew. Chem., Int. Ed.* **2009**, *48*, 8832−8846.
(45) Giordano, G.; Crabtree, R. H.; Heintz, R. M.; Forster, D.; Morris, D. E. *Inorg. Synth.* **1990**, *28*, 88−90.
(46) Harris, R. K.; Becker, E. D.; Cabral De Menezes, S. M.; Granger, P.; Hoffman, R. E.; Zilm, K. W. *Pure Appl. Chem.* **2008**, *80*, 59−84.
(47) Connelly, N. G.; Geiger, W. E. *Chem. Rev.* **1996**, *96*, 877−910.
(48) *APEX2*, Version 2008.3-0, or (Version 2.2-0); Bruker AXS, Inc.; Madison, WI, 2007.
(49) *SAINT*, Version 7.53a (or 7.46a); Bruker AXS, Inc.: Madison, WI, 2007.
(50) Sheldrick, G. M. *SADABS*, Version 2007/4; Bruker AXS, Inc.: Madison, WI, 2007.
(51) Sheldrick, G. M. *SHELXTL*, Version 6.12; Bruker AXS, Inc.: Madison, WI, 2001.
(52) *International Tables for X-Ray Crystallography*; Kluwer Academic Publishers: Dordrecht, The Netherlands, 1992; Vol. *C*.
(53) Farrugia, L. J. *J. Appl. Crystallogr.* **1997**, *30*, 565.
(54) Gans, P.; Sabatini, A.; Vacca, A. *HYPERQUAD2003*; University of Leed and University of Florence: Leeds, U.K., and Florence, Italy, 2003.
(55) Gans, P.; Sabatini, A.; Vacca, A. *Talanta* **1996**, *43*, 1739−1753.
(56) TURBOMOLE GmbH: Karlsruhe, Germany.
(57) Becke, A. D. *J. Chem. Phys.* **1993**, *98*, 1372−1377.
(58) Lee, C.; Yang, W.; Parr, R. G. *Phys. Rev. B.* **1988**, *37*, 785−789.
(59) Vosko, S. H.; Wilk, L.; Nusair, M. *Can. J. Phys.* **1980**, *58*, 1200−1211.
(60) Stephens, P. J.; Devlin, F. J.; Cabalowski, C. F.; Frisch, M. F. *J. Phys. Chem.* **1994**, *98*, 11623−11627.
(61) Weigend, F.; Ahlrichs, R. *Phys. Chem. Chem. Phys.* **2005**, *18*, 3297.
(62) Reed, A. E.; Weinstock, R. B.; Weinhold, F. *J. Chem. Phys.* **1985**, *83*, 735−746.
(63) Klein, R. F. X.; Bargas, L. M.; Horak, V. *J. Org. Chem.* **1988**, *53*, 5994−5998.
(64) Dutta, S.; Basuli, F.; Peng, S.-M.; Lee, G.-H.; Bhattacharya, S. *New J. Chem.* **2002**, *26*, 1607−1612.
(65) Baksi, S.; Acharyya, R.; Dutta, S.; Blake, A. J.; B., D. M. G.; Bhattacharya, S. *J. Organomet. Chem.* **2007**, *692*, 1025−1032.
(66) Blacker, A. J.; Clot, E.; Duckett, S. B.; Eisenstein, O.; Grace, J.; Nova, A.; Perutz, R. N.; Taylor, D. J.; Whitwood, A. C. *Chem. Commun.* **2009**, 6801−6803.
(67) Acharya, K. R.; Tavale, S. S.; Guru Row, T. N. *Acta Crystallogr.* **1984**, *C40*, 1327−1328.
(68) Hughes, R. P.; Lindner, D. C.; Liable-Sands, L. M.; Rheingold, A. L. *Organometallics* **2001**, *20*, 363−366.
(69) Egan, J. W. Jr.; Hughes, R. P.; Rheingold, A. L. *Organometallics* **1987**, *6*, 1578−1581.
(70) Choi, J.-C.; Sakakura, T. *J. Am. Chem. Soc.* **2003**, *125*, 77762−77763.
(71) Nishihara, Y.; Nara, K.; Nishide, Y.; Osakada, K. *J. Chem. Soc., Dalton Trans.* **2004**, 1366−1375.
(72) Allen, F. H.; Kennard, O.; Watson, D. G.; Brammer, L.; Orpen, A. G.; Taylor, R. *J. Chem. Soc., Dalton Trans. II* **1987**, S1−S19.
(73) Osakada, K.; Ishii, H. *Inorg. Chim. Acta* **2004**, *357*, 3007−3013.
(74) Kuznetsov, V. F.; Yap, G. P. A; Bensimon, C.; Alper, H. *Inorg. Chim. Acta* **1998**, *280*, 172−182.
(75) de Pater, B. C.; Frühous, H.-W.; Vrieze, K.; de Gelder, R.; Baerends, E. J.; McCormack, D.; Lutz, M.; Spek, A. L.; Hartl, F. *Eur. J. Inorg. Chem.* **2004**, 1675−1686.
(76) Youssef, T. E. *Polyhedron* **2010**, *29*, 1776−1873.
(77) Chou, M.; Creutz, C.; Mahajan, D.; Sutin, N.; Zipp, A. P. *Inorg. Chem.* **1982**, *21*, 3989−3997.
(78) Martin, B.; McWhinnie, W. R.; Waind, G. M. *J. Inorg. Nucl. Chem.* **1961**, *23*, 207−223.
(79) Cissell, J. A.; Vaid, T. P.; Yap, G. P. A. *J. Am. Chem. Soc.* **2007**, *129*, 7841−7847.
(80) Storr, T.; Wasinger, E. C.; C., P. R.; Stack, D. P. *Angew. Chem., Int. Ed.* **2007**, *46*, 5198−5201.